Manipulating solid-state spin concentration through charge transport

Guoqing Wang[a,b,1] (ID), Changhao Li[a,b,2] (ID), Hao Tang[c] (ID), Boning Li[a,d], Francesca Madonini[a,e], Faisal F. Alsallom[d], Won Kyu Calvin Sun[a] (ID), Pai Peng[f], Federica Villa[e], Ju Li[b,c,1] (ID), and Paola Cappellaro[a,b,d,1] (ID)

Solid-state defects are attractive platforms for quantum sensing and simulation, e.g., in exploring many-body physics and quantum hydrodynamics. However, many interesting properties can be revealed only upon changes in the density of defects, which instead is usually fixed in material systems. Increasing the interaction strength by creating denser defect ensembles also brings more decoherence. Ideally one would like to control the spin concentration at will while keeping fixed decoherence effects. Here, we show that by exploiting charge transport, we can take some steps in this direction, while at the same time characterizing charge transport and its capture by defects. By exploiting the cycling process of ionization and recombination of NV centers in diamond, we pump electrons from the valence band to the conduction band. These charges are then transported to modulate the spin concentration by changing the charge state of material defects. By developing a wide-field imaging setup integrated with a fast single photon detector array, we achieve a direct and efficient characterization of the charge redistribution process by measuring the complete spectrum of the spin bath with micrometer-scale spatial resolution. We demonstrate a two-fold concentration increase of the dominant spin defects while keeping the T_2 of the NV center relatively unchanged, which also provides a potential experimental demonstration of the suppression of spin flip-flops via hyperfine interactions. Our work paves the way to studying many-body dynamics with temporally and spatially tunable interaction strengths in hybrid charge–spin systems.

charge dynamics | spin defects | double electron–electron resonance | NV centers | charge transport

Defects in solid state material have become promising quantum information platforms in developing quantum sensors (1, 2), memories (3), networks (4), and simulators (5, 6). In addition to the spin degrees of freedom that are most often used due to their valuable quantum coherence and controllability, the charge degree of freedom attracts increasing interest due to its influence on the spin state and potential in characterizing and tuning spin and charge environment (7, 8). The charge state can be manipulated and probed through either optical illumination (9, 10) or electrical gates (11–13), and it can also serve as a meter to yield information about the environment (14–17). Combining these control and detection methods, charge transport has been observed in diamonds with both sparse (18) and dense (19) color centers. Moreover, nonfluorescent dark charge emitters can be imaged through carrier-to-photon conversion (20, 21), and the spin-to-charge conversion has enabled single-shot spin readout (22–24).

In this work, we show that charge transport can be used to manipulate the spin concentration in materials. Under optical illumination, the in-gap material defects undergoing cycling transitions of ionization and recombination can continuously pump electrons from the valence band (VB) to the conduction band (CB). Then, the electrons diffuse and get captured by other in-gap defects, whose variation in charge state modulates their spin states, thus affecting both the spin and charge environment simultaneously. With a home-built wide-field imaging microscope integrated with a fast single photon detector array and a two-beam pump–probe setup, we observe the charge pumping and redistribution among different spin defects. By characterizing the double electron–electron resonance (DEER) spectrum using NV centers in diamond, we show that the concentration of the dominant paramagnetic (S = 1/2) nitrogen defect, the P1 center, can be increased by a factor of 2, while an additional, unknown-type electron spin density can be decreased by a factor of 2.

Tuning the Spin Density through Charge Transport

The sample we study is a diamond grown using chemical vapor deposition (CVD) by Element Six with ~10 ppm ^{14}N concentration and 99.999% purified ^{12}C. Various

Significance

Solid-state spin defects are promising platforms for quantum sensing and simulation. Although their spin degrees of freedom have been extensively studied, their charge states are also of critical interest as they set the defect spin and influence their coherence time. Here, we exploit nitrogen-vacancy center photoionization and charge transport to tune the density of the P1 spins in diamonds. Using the NVs as quantum sensors of their spin and charge environment, we demonstrate a 2x increase in the P1 concentration, while preserving the quantum sensor coherence. The charge redistribution is imaged by a wide-field imager by measuring the spin bath spectrum.

in-gap point defects including nitrogen-vacancy (NV) centers are generated through electron irradiation and subsequent annealing at high temperature. The energy gap of a diamond is 5.5 eV, prohibiting pumping electrons from the VB to CB through a one-photon process with visible light sources around 2 eV. Instead, such a pumping can be assisted by these in-gap defects including the NV centers (18, 19). Under laser illumination with sufficient energy, the ionization of the negatively charged NV^- is a two-photon process: It is first pumped to its excited state and is further ionized to NV^0 by transferring one electron to the diamond CB. The recombination of NV^0 is through a similar two-photon process with the second step pumping an electron from the valence band to convert the center back to NV^- (9). Such a cycling process generates a stream of electrons and holes in the conduction and valence bands respectively as shown in Fig. 1A, which will subsequently transport diffusively to locations a few micrometers away in a time scale from milliseconds to seconds (18, 19).

In addition to photoionization, the conversion between different charge states can happen through direct electron or hole capture. Accounting for all these effects, the densities of the negative NV charge states, Q_-, e.g., satisfy the equation $\frac{dQ_-}{dt} = -k_- Q_- + k_0 Q_0 + \kappa_n n Q_0 - \kappa_p p Q_-$, where Q_0 is the neutral NV density, k_-, k_0 are photoionization rates, κ_n, κ_p are the electron trapping (releasing) rates, and n, p are the densities of electrons and holes. Similar equations apply to other defects with the corresponding rate constants set by the laser intensity and wavelength, as well as the charge state energies with respect to the CB and VB. The dynamics of the defect density distribution is further determined by including the modified diffusion equation for the electron and holes, e.g., $\frac{dn}{dt} = D_n(\partial^2 n/\partial r^2 + (1/r)\partial n/\partial r) + (e^- \text{ pumping} - e^- \text{ capture})$, where the last two terms describe the total rates of electron generation (pumping) and absorption (capture) in the material, for example, due to photo(de)ionization or direct electron/hole capture process.

When considering an (quasi-)equilibrium condition with (quasi-)static charge state density, the charge state distribution is set by the local electron and hole densities, as well as the photoionization rate, which can be controlled through photoionization process. In this work, we focus on studying the substitutional nitrogen defects N_s^0 and N_s^+, where the neutral charge state N_s^0 (P1 center) has a spin $S = 1/2$ and the positive charge state N_s^+ has no spin. In a typical CVD diamond, the density of these defects is usually one to two orders of magnitude larger than NV centers, thus contributing to the dominant spin bath (25).

Following the rate model above, the spin density can be obtained from $n[N_s^0] = n[N_s]\frac{\gamma_n n}{\gamma_n n + \gamma_p p + k_N}$, where constant γ_n, γ_p are electron (hole) capture rates and k_N is the P1 photoionization rate only $N_s^0 \to N_s^+$ is considered due to insufficient laser energy for the inverse process in our experiment (19, 26). Then, the spin density $n[N_s^0]$ can be tuned through both the photoionization rate k_N and the local charge densities n, p, in turn controlled by the NV charge cycling process and by charge transport. Previous studies have reported that the $n[N_s^+]$ in CVD diamond is typically 1 to 10 times more abundant than $n[N_s^0]$ (27), indicating a potentially large tunable range for $n[N_s^0]$.

Probing the Spin Environment with DEER

To probe the electronic spin environment with high resolution over both spatial and frequency domains, we combine our new imaging setup with DEER control techniques.

We built a wide-field imaging setup (28) integrated with a fast single photon avalanche diode (SPAD) array (29) with a 100-kHz frame rate and 32×64 pixels (30), as shown in Fig. 1B. A narrow laser beam ($D \sim 32\,\mu m$, 0.5 W) is used for charge pumping, whereas a broad laser beam ($D \sim 200$ to $500\,\mu m$, 0.6 W) is used for fluorescence readout. A static magnetic field $B = 239$ G is aligned along one of the four NV orientations. To probe the various spin species interacting with our NV ensemble, we apply the DEER sequence (inset of Fig. 1C) to perform spectroscopy of the spin bath. As shown in Fig. 1C, the spectrum shows that, in addition to the expected P1 centers, a substantial concentration of extra (Ex) defects exist with resonance near $g = 2$.
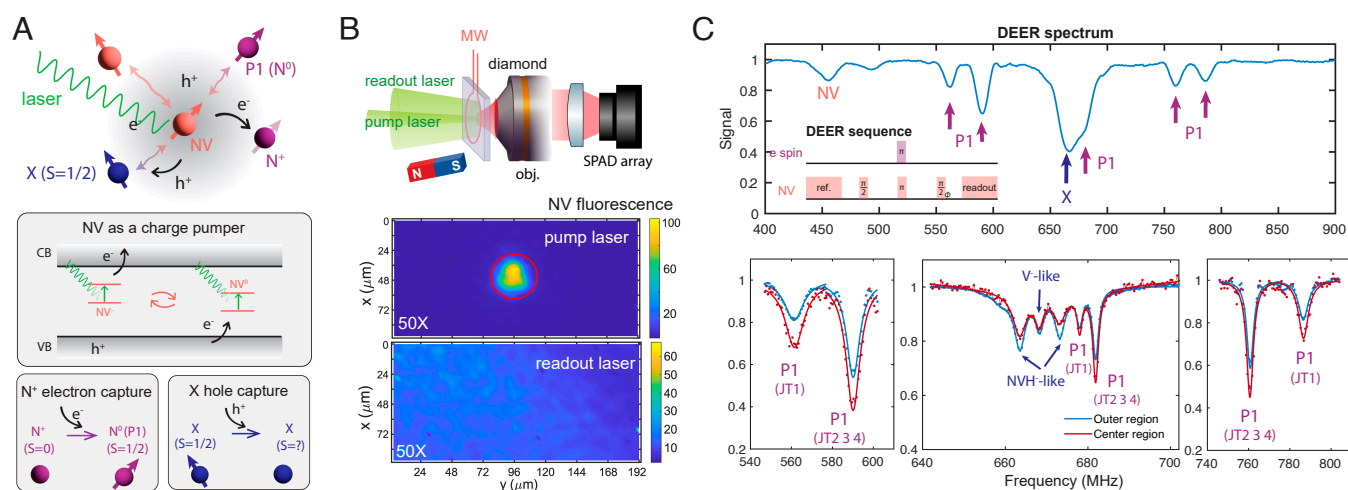
Fig. 1. Tuning the spin density via charge variations. (A) Charge state conversion under laser illumination in a system containing different spin defects (*Top*). The charge dynamics is influenced by laser illumination and electron/hole captures by different species (*Bottom*) (B) Schematic of the experimental setup (*Top*) and corresponding NV fluorescence imaging (*Bottom*) under the illumination of the focused laser beam and the broad laser beam. (C) DEER spectra when both pump and readout lasers are on for 0.4 ms in each repetition (Fig. 2). The *Upper* panel shows the measurement under a strong π pulse power ($t_\pi = 0.074\,\mu s$, calibrated for the 560 MHz P1 resonance frequency). The *Bottom* three panels show the measurements under a selective π pulse with low power (calibrated separately for each resonance frequency). Dark red curves show the total SPAD signal within the red circle shown in *B*, while the blue curves show the SPAD signal outside the circle, indicating different concentrations of the spin defects.

To study the effect of our controlled charge pumping process (via controlled NV illumination), we analyze the spin concentration quantitatively from the DEER measurements. In the DEER experiment (Fig. 2A), the NV acts as a probe of the magnetic noise generated by the component of the spin bath that is resonantly driven. More specifically, while the spin echo sequence (alone) applied on the NV cancels out the interaction with the entire electronic spin bath, the addition of a spin flip pulse close to a particular bath-spin resonance recouples the interaction with only the corresponding spin species. The signal decay is then composed of a Ramsey-like dephasing characterized by T_s^*, due to interaction with the recoupled spin species, and an echo-like decay due to the other spin species, with characteristic time $\sim T_2$. Thus, the DEER signal has a form $I_{\text{DEER}} = \exp(-T/\tau)$ with $1/\tau = 1/T_s^* + 1/T_2$, where T is the free evolution time. The dephasing time T_s^* due to a given spin species s can be calculated from the rms noise field acting on the NV center due to the spin dipolar coupling (31, 32), yielding

$$\frac{1}{T_s^*} = \frac{2\pi\mu_0\mu_B^2\, g_A g_s |\sigma|}{9\sqrt{3}\hbar} P_s n_s = 0.1455 n_s, \, [\mu s^{-1}] \qquad [1]$$

where g_A, g_s are g-factors for the central and bath spins, and n_s is the concentration of the spin species s. P_s describes the probability to invert the spin population, and we set $P_s = 1$ assuming that the π pulse for the spin-flip operation is perfect, and bath spins are assumed to be spin-1/2, thus $|\sigma| = 1/2$. Here, T_s^* is in units of μs and n_s is in units of ppm.

To extract the bath spin density n_s, we experimentally measure the NV coherence time τ under the DEER sequence for each resonance frequency of bath spin species and fit the exponential decay to the analytical formula, I_{DEER}. By comparing to the measured NV spin echo coherence time T_2, we extract the value of T_s^*, from which we obtain the density of the recoupled spin species n_s. In Fig. 2B, we show an example of the comparison of time evolution experiments with (blue) and without (gray) recoupling pulse, and with pump laser illumination (red). The measurements show clear differences in both the coherence times and signal contrast, revealing the different bath spin density and NV ionization fraction (see *SI Appendix* for more details).

Redistribution of Electronic Spin Species under Laser Illumination

Applying the above techniques to probe our sample with moderate native spin densities and sufficiently coherent NV ensemble, we report a high-resolution DEER spectrum around $g = 2$ which reveals a (reproducible) redistribution of the electronic spin species in diamond under laser illumination. Concretely, a low-power DEER spectrum reveals multiple resonances (labeled Peak 1 to 6 in Fig. 2E), which includes not only the known P1 (Peak 5 to 6) but also additional resonances (Peak 1 to 4) belonging to spins dubbed X defects in the literature (31). Thus, comparing the DEER spectra with and without the strong focused green laser reveals redistribution of spin species with a preferential increase for P1 and decrease for X, shown in Figs. 2 C, D, and F.

Controlled variations in the spin bath density are a useful resource for quantum simulation of many-body physics, as recently proposed (5). Concretely, to further enhance the quantum simulation capability of NV-P1 systems, we would like to add: i) a tunable knob over [P1] that is also stable for the duration of a typical quantum simulation (μs-ms), which, however ii) leaves intact the coherence properties of the NV centers. The former capability increases the range of interaction strengths that can be explored in the quantum simulator, while the latter will at least keep the same circuit depth/simulation time despite the cost of enacting (i) which physically leads to a nonequilibrium complex charge environment.
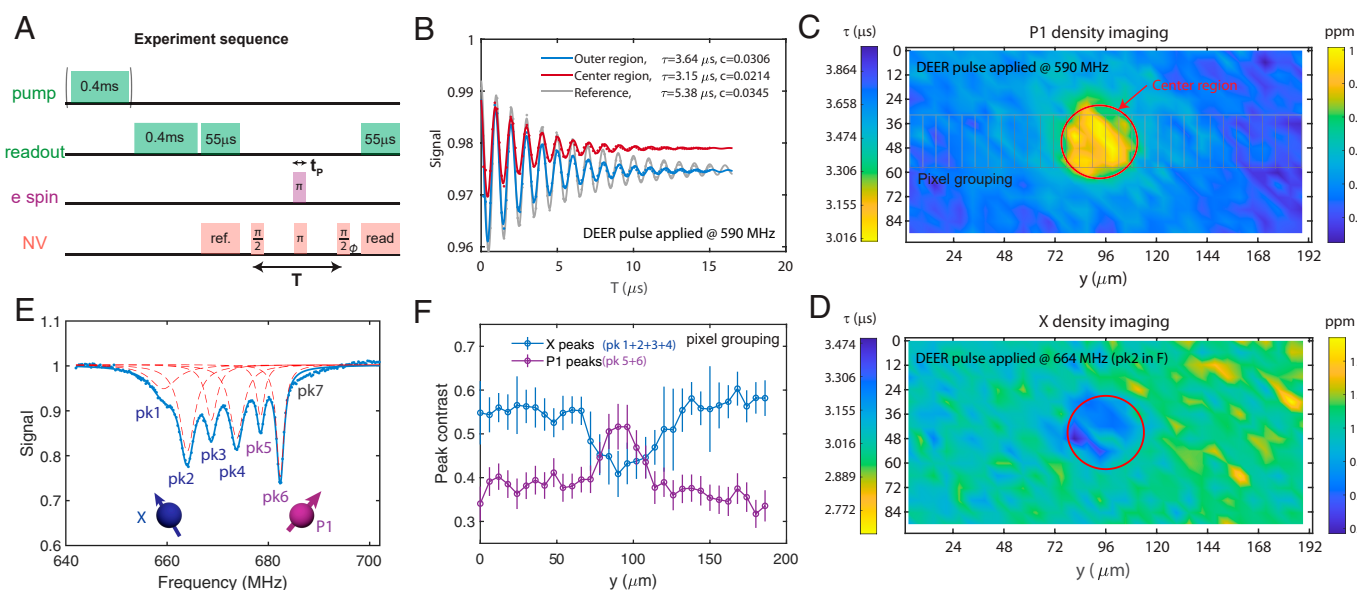
Fig. 2. Redistribution of electronic spin species under illumination. (*A*) Control sequence for charge generation and DEER experiments. (*B*) Time evolution of the NV signal under DEER in different sample regions. The red curve is the total signal inside the circle shown in (*C*), while the blue curve is from outside the circle. The gray curve is the NV spin echo, that is, without applying the bath π pulse. All the time-dependent signals are fit to an exponential decay $S(T) = \frac{c}{2}e^{-T/\tau}\cos(d\omega T + \phi_0) + c_0$, where $\phi = d\omega T$ is a time-dependent phase applied to the last NV $\pi/2$ pulse to modulate the signal. We set $d\omega = (2\pi)1$ MHz in all similar experiments in this work. From the fit we extract the signal contrast c and decay time τ. (*C* and *D*) Imaging of P1 and X density, n_s, obtained (Eq. **1**) from the measured DEER coherence time, $T_s^* = (1/\tau - 1/T_2)^{-1}$, with the bath π pulse applied at 590 and 664 MHz, respectively. Here $T_2 = 5.375$ μs is the NV spin echo coherence time measured by the reference experiment (gray curve in *B*). (*E*) Representative DEER spectrum with high-frequency resolution. We group the measured pixel signal as shown by the gray rectangles in *C* to achieve a better signal-to-noise ratio. The signal is then fit to six Lorentzian peaks shown by the red dashed lines. (*F*) Extracted peak heights from (*E*) as a function of the y position.

We now show that we can take steps toward realizing these two goals via the NV charge cycling and transport process.

Tunable and Stable P1 Concentration in the Dark. In order to be useful for quantum simulations, we should be able to change the density of spin defects with illumination but then maintain it at a stable level over the spin dynamics characteristic timescale (from µs to ms given typical dipolar interaction strength of MHz to kHz). To verify that the charge state can be treated as quasi-static thanks to its long recovery timescale in the dark (previously evaluated to be due on the ms to seconds timescale) (18, 19), we experimentally characterize the charge dynamics including both the generation and recovery processes using the sequence shown in Fig. 3A. After a fast photoinduced charge initialization process (characteristic timescale less than 0.05 ms), the charge state shows a long recovery time, more than tens of ms, as shown in Fig. 3 B and C. Our results demonstrate the feasibility and flexibility of manipulating the spin concentration using charge transport in a quasi-static way. We note that the measurement of the recovery shape and rate is a characterization of the underlining material properties including charge mobility, capture cross-section, tunneling rate, etc. Further quantitative explanations of such a process require a more comprehensive study combining different experimental probes and theoretical insights.

Coherence Time under Varying Spin Density. The coherence times of NV centers are influenced by the redistribution of the spin density.

The coherence time of a central single spin (NV) interacting with a dipolar spin bath can be estimated by assuming the bath generates a classically fluctuating field (33). The central spin coherence time under free evolution (Ramsey dephasing) is then $T_2^* = \frac{\sqrt{2}}{\gamma_e \sqrt{\langle B_1^2 \rangle}}$, while evolution under a spin echo lead to a coherence time $T_2 = \left(\frac{12\tau_c}{\gamma_e^2 \langle B_1^2 \rangle} \right)^{1/3}$. The mean strength of the noise field $\sqrt{\langle B_1^2 \rangle}$ is proportional to the spin density, and the correlation time τ_c is set by the flip-flop interaction between resonant bath spins. Combining the analysis of T_2 and T_2^* provides a characterization of both the density and the correlation of the spin bath (34) as shown in Fig. 4A. In Fig. 4 B–D, we measure the spatial distribution of both T_2^* and T_2 with the pump laser illumination applied to the central region. The experimental results show that even though T_2^* decreases in the central region due to the increase in the total spin densities (composed of the increase of P1 density and the decrease of NVH-like defect density), T_2 remains relatively unchanged for all regions.

One potential explanation for such an intriguing phenomenon is based on the suppression of flip-flop rates of different spin species due to hyperfine interactions and Jahn–Teller (JT) orientations, which introduce energy mismatch in the two-spin flip-flop subspace. Such an effect was discussed in refs. 33 and 35 and was recently revealed by first-principles calculations in ref. 36. In the flip-flop subspace spanned by the states $|0\rangle = |\uparrow\downarrow\rangle$ and $|1\rangle = |\downarrow\uparrow\rangle$, the interaction Hamiltonian is simplified to $H_{sub} = \delta\sigma_z + C_\perp\sigma_x$ with 2δ the energy difference between states $|0\rangle$ and $|1\rangle$ and $C_\perp$ the transverse coupling strength. Taking into account the dephasing rate Γ_d, the bath correlation time τ_c is then given by $1/\tau_c \sim R_{ff,0}^{ij} = (C_\perp^{ij})^2 \Gamma_d / (\Gamma_d^2 + \delta^2)$ (33). The different nuclear spin states and JT orientations $|m\rangle$ suppress the flip-flop rate as they induce the energy mismatch δ_m between $|\uparrow\downarrow\rangle \otimes |m_1\rangle$ and $|\downarrow\uparrow\rangle \otimes |m_2\rangle$ ($\delta_m \gg \Gamma_d$). Intuitively,

we can define a suppression factor α, in comparison to the unsuppressed flip-flop rate $R_{ff,0}$, by summing over all cases of $|m\rangle$ such that $R_{ff}^{ij} = \frac{(C_\perp^{ij})^2}{\Gamma_d} \sum_m \frac{1}{M} \frac{\Gamma_d^2}{(\Gamma_d^2 + \delta_m^2)} = \alpha R_{ff,0}^{ij}$. M is the number of nuclear spin states and JT orientations as shown in Fig. 4E*. Numerical calculations give the suppression factors for different spin defects $\alpha_{P1} \approx 0.208$, $\alpha_{NVH} \approx 0.353$ assuming $\Gamma_d = (2\pi)1$ MHz (see *SI Appendix* for different approaches to calculating α).

With large hyperfine interaction, the electronic spin flip-flop of P1 is more suppressed than other defects, especially those appearing near $g = 2$. Thus, the contribution to the change of T_2 time due to density decrease of NVH-like spin defects (~2.5 ppm to ~1.6 ppm, extracted from Fig. 2D which contributes ≲ 1/2 of the total NVH-like defect density) could compensate the larger amount of P1 increase (~2 ppm to ~4 ppm, extracted from Fig. 2C, which contributes 1/4 of the total P1 density). Our experiments present an observation of different suppressions of the noise contribution as predicted by the recent work (36). We note that the measured T_2^* in Fig. 4C is shorter than what we predict from the total spin density (T_2^* is predicted to be ~1.1 µs for the outer region given by the characterized spin densities). We attribute such a discrepancy to the magnetic or electric field inhomogeneity generated by the charge transport, which creates a local current induced by the laser on–off during the sequence repetitions and electron–hole separation due to their different diffusion constants (see *SI Appendix*, 37, 38).

Discussion on the Identification of X

Even though we cannot uniquely identify the X spins, we can still draw a few conclusions based on experiments and theoretical calculations. Peaks 1, 2, 4 in Fig. 1C and Fig. 2F show a larger contrast decrease in the central region than peak 3 at the $g = 2$ frequency. The widths and contrasts of peaks 2, 4 are similar, and both are larger than peak 3. Based on this, we conclude that we have at least two spin species, peaks 1, 2, 4 belonging to X1 and peak 3 belonging to X2. Comparing the spectrum features with simulations shown in *SI Appendix* based on reported values of various spin defects in CVD diamond (25, 39–45), X1 is possibly the NVH$^-$ defect and X2 can be any $g = 2$ spin defect without hyperfine splitting, such as a simple vacancy V$^-$ (or a spin with a weak hyperfine such as VH$_2^-$). Different from the increase of P1 due to the electron capture of the N$_s^+$, the decrease of X1 and X2 can be induced by the hole capture process or direct photoionization. For NVH$^-$, the hole capture process converts it to a spin-1 state NVH^0. Using first-principle calculations, we obtain the zero-field splitting of NVH^0 as $D = 2.290$ GHz, which predicts the spin resonance frequencies. However, no significant signals are observed at these frequencies, potentially indicating the defect (if it indeed exists) is further ionized (see *SI Appendix*). Indeed, the laser energy 532 nm = 2.33 eV used in our experiment is larger than the first-principle predicted excitation (1.603 eV) and ionization (2.27 eV) energies for NVH^0. Further identification of these defects can be achieved by varying the excitation laser frequencies to characterize their transition energies and comparing them to first-principles calculations of the defect energy levels. We note that the NVH defects are common in CVD-growth diamonds due to the use of CH$_4$/H$_2$ gas mixtures in the

---

*Here, we assume that the nuclear spin is in a fully mixed state such that different states $|m\rangle$ contribute in an equal probability. The magnetic field is aligned along JT1 orientation such that JT2, 3, 4 orientations are degenerate.
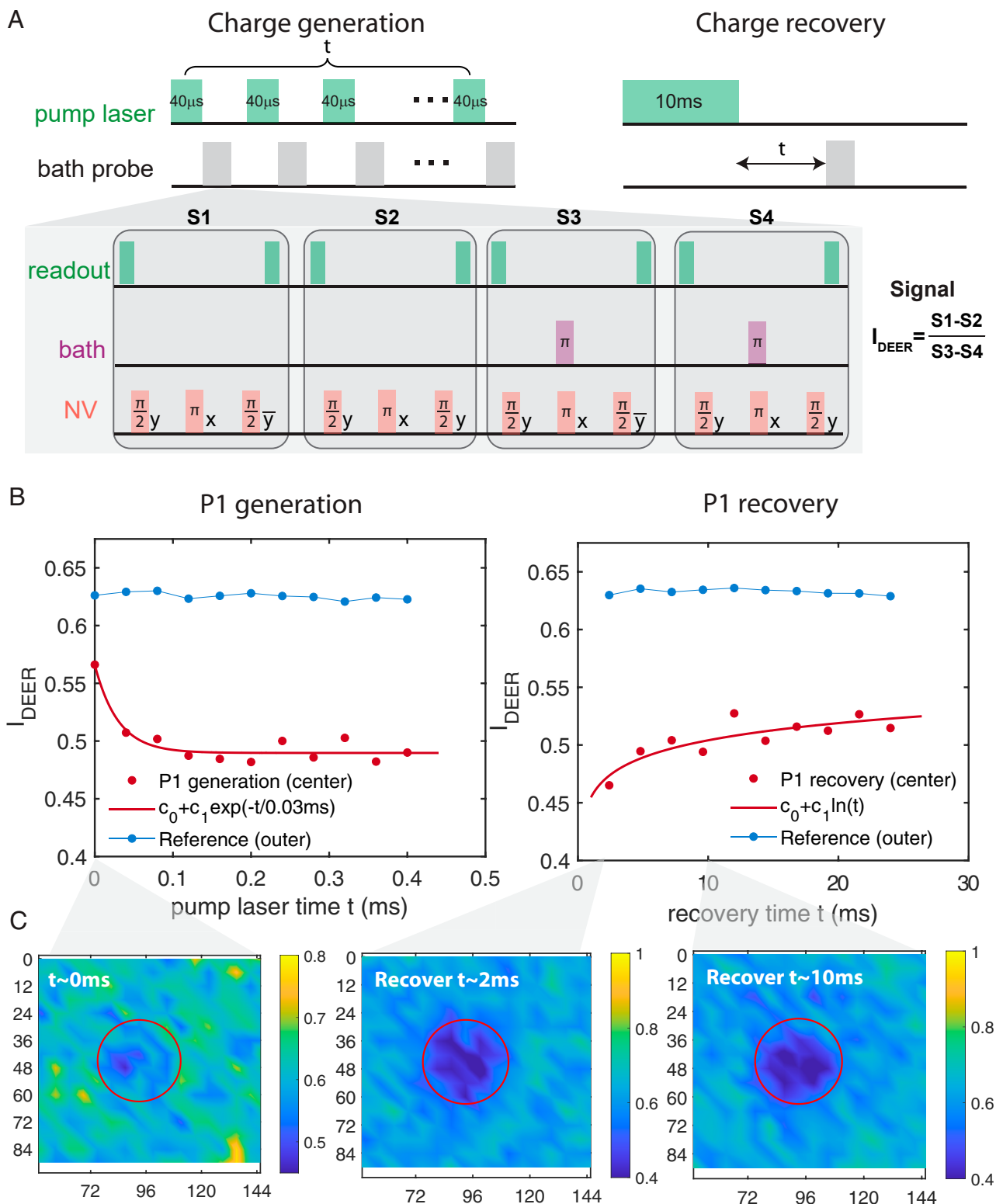
Fig. 3. Lifetime of charge states. (*A*) Experimental sequence to probe the charge dynamics. To measure the generation of charges via their effect on P1 density, we apply a short 40-μs pump laser pulses to better capture the fast charge-generation process. The laser is followed by an echo and a DEER sequence that measure the P1 concentration (DEER) and calibrates it against the NV coherence (echo). The echo/DEER is further calibrated by repeating the sequence with a different phase of the last π/2 pulse. A 0.126-μs π pulse is applied to probe the P1 on resonance at 590 MHz. To measure the charge recovery, a single long pump laser illumination of 10-ms duration (to ensure sufficient charge generation and transport) is followed by repeated echo/DEER sequences, and a long wait time of 0.2 s is used between different repetitions to ensure sufficient charge recovery. The broad beam is used for readout, and its effects on charge dynamics can be neglected due to the low intensity. (*B*) Evolution of the DEER contrast I_{DEER} in the central (red circle in *C*) and outer regions during and after the charge pumping. (*C*) The contrast I_{DEER} at various recovery times. All experiments in this figure are performed with 160,000 repetitions.
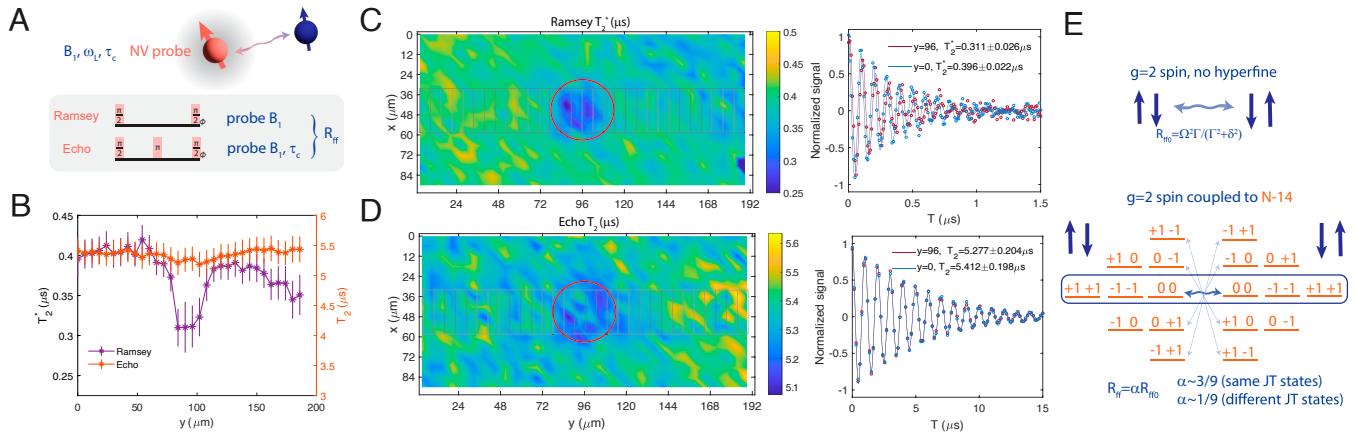
Fig. 4. Coherence time imaging. (*A*) Ramsey and echo sequences to probe the spin density and flip-flop rates of the spin bath surrounding the NV probe. (*B*) Coherence time under Ramsey and echo experiments. The complete sequence, including laser pulses, is similar to Fig. 2*A*. Each data point is the fitted decay time τ of the total signal in grouped pixels shown (*C* and *D*). The grouped pixel signal is fit to $S(T) = \frac{c}{2}e^{-T/\tau}\cos(d\omega T + \phi_0) + c_0$, and the error bars in the plot show the 95% confidence intervals of fitting parameters extracted from the fitting result. (*C*) Ramsey coherence time T_2^* imaging. A large coherence-time decrease is observed in the pump beam region (see the range of the color bar). (*D*) Echo coherence time T_2 imaging. A small coherence-time decrease is observed in the central region. (*E*) Analytical model for the suppression of the electronic spin flip-flop rate.

diamond growth (40), and vacancies can be generated during the electron irradiation and annealing process to form NV centers (46, 47).

Discussions and Conclusions

We propose and demonstrate the manipulation of spin concentration in diamonds through charge transport. Making use of the redistribution of the photoinduced charges over different spin species with different flip-flop suppression, the coherence time of the probe (NV) spin is relatively unchanged. Besides characterizing the steady states of the system under repetition of the sequence, we demonstrate the feasibility of characterizing the charge dynamics. Our work provides a flexible tool to characterize materials, including both the charge and spin dynamics by measuring the DEER spectrum.

In recent years, solid-state defects have shown potential in exploring hydrodynamics, aiming to bridge the gap between microscopic quantum laws and macroscopic classical phenomena (5). The natural dipolar interactions in the spin ensemble serve as a versatile platform to engineer and characterize many-body quantum spin systems (5, 48). Our work provides approaches to temporally and spatially tune the spin concentration in these spin transport experiments in the same material while maintaining the spin coherence time. Moreover, introducing the charge degree of freedom into the system provides a more flexible platform to engineer a many-body system with two coupled transport mechanisms (5, 49, 50). For example, with the capability of reading out an array of pixels in a fast and parallel manner, our experiment provides a platform to study the spin transport described by $\partial_t P(t, \vec{r}) = D(t, \vec{r})\nabla^2 P(t, \vec{r}) - P(t, \vec{r})/T_1 + Q(t, \vec{r})$ with a temporally and spatially varying diffusivity $D(t, \vec{r})$.

Further integrating our setup with a wavelength-tunable laser could reveal the defect energy levels with respect to the material energy bands more precisely, allowing the identification of various defects when combining experiments with first-principles calculations. Such a fingerprint enables a more complete reconstruction of the local charge and spin environment (12, 51, 52). Combining the charge density control

with spin-to-charge conversion (53) paves the way to coherent transport of quantum information through charge carriers (49) and on-demand generation of other quantum spin defects (54). Besides, improving the optical tunability of local charge density is promising for developing charge lens through laser beam patterning (55).

Materials and Methods

Ab Initio Calculations of the Vacancy Defect Spin Hamiltonian. We implemented ab initio calculations of the NVH^0 and VH_2^0 defects in diamond. The defect structure is simulated by the supercell method (56) using a $3 \times 3 \times 3$ cubic supercell (with 216 atoms). The calculation used density functional theory (DFT) and projector-augmented wave (PAW) method carried out through Vienna *abinitio* simulation package (VASP) (57, 58). A generalized gradient approximation is used for exchange-correlation interaction with the PBE functional (59). The cutoff energy is set as 400 eV, and a $3 \times 3 \times 3$ k-point mesh is sampled by the Monkhorst–Pack scheme (60). The defect structure is fully relaxed with a residue force on each atom less than 0.01 eV/Å, and the electronic energy converges to 10^{-7} eV. The zero-field splitting is then calculated from the DFT electronic ground state using (61):

$$D_{ab} = \mu_0 g_e^2 \beta^2 \sum_{i<j}^{p+q} \chi_{ij} \langle \Psi_{ij}(\mathbf{r}_1, \mathbf{r}_2) | \frac{r^2 \delta_{ab} - 3r_a r_b}{r^5} | \Psi_{ij}(\mathbf{r}_1, \mathbf{r}_2) \rangle.$$

The calculated D_{ab} of NVH^0 is

$$D_{ab}(NVH^0) = \begin{bmatrix} -0.76 & 0 & 0 \\ 0 & -0.76 & 0 \\ 0 & 0 & 1.53 \end{bmatrix} \text{GHz},$$

where the z-axis is set as the C_{3v} axis of NVH^0. The calculated D_{ab} of VH_2^0 in the cubic axis (the axis is along the three lattice vectors of the cubic supercell of diamond, and we make the two hydrogen atoms in xz-plane) is:

$$D_{ab}(VH_2^0) = \begin{bmatrix} -0.40 & 0 & 2.21 \\ 0 & 0.79 & 0 \\ 2.21 & 0 & -0.40 \end{bmatrix} \text{GHz},$$

Author affiliations: [a]Research Laboratory of Electronics, Massachusetts Institute of Technology, Cambridge, MA 02139; [b]Department of Nuclear Science and Engineering, Massachusetts Institute of Technology, Cambridge, MA 02139; [c]Department of Materials Science and Engineering, Massachusetts Institute of Technology, Cambridge, MA 02139; [d]Department of Physics, Massachusetts Institute of Technology, Cambridge, MA 02139; [e]Dipartimento di Elettronica, Informazione e Bioingegneria, Politecnico di Milano, Milano 20133, Italy; and [f]Department of Electrical Engineering, Princeton University, Princeton, NJ 08544

1. J. R. Maze et al., Nanoscale magnetic sensing with an individual electronic spin in diamond. *Nature* **455**, 644–647 (2008).
2. J. M. Taylor et al., High-sensitivity diamond magnetometer with nanoscale resolution. *Nat. Phys.* **4**, 810–816 (2008).
3. A. Ruskuc, C. J. Wu, J. Rochman, J. Choi, A. Faraon, Nuclear spin-wave quantum register for a solid-state qubit. *Nature* **602**, 408–413 (2022).
4. M. Pompili et al., Realization of a multinode quantum network of remote solid-state qubits. *Science* **372**, 259–264 (2021).
5. C. Zu et al., Emergent hydrodynamics in a strongly interacting dipolar spin ensemble. *Nature* **597**, 45–50 (2021).
6. G. Wang, C. Li, P. Cappellaro, Observation of symmetry-protected selection rules in periodically driven quantum systems. *Phys. Rev. Lett.* **127**, 140604 (2021).
7. F. Dolde et al., Nanoscale detection of a single fundamental charge in ambient conditions using the NV - center in diamond. *Phys. Rev. Lett.* **112**, 097603 (2014).
8. S. Dhomkar, H. Jayakumar, P. R. Zangara, C. A. Meriles, Charge dynamics in near-surface, variable-density ensembles of nitrogen-vacancy centers in diamond. *Nano Lett.* **18**, 4046–4052 (2018).
9. N. Aslam, G. Waldherr, P. Neumann, F. Jelezko, J. Wrachtrup, Photo-induced ionization dynamics of the nitrogen vacancy defect in diamond investigated by single-shot charge state detection. *New J. Phys.* **15**, 013064 (2013).
10. S. Dhomkar, P. R. Zangara, J. Henshaw, C. A. Meriles, On-demand generation of neutral and negatively charged silicon-vacancy centers in diamond. *Phys. Rev. Lett.* **120**, 117401 (2018).
11. B. Grotz et al., Charge state manipulation of qubits in diamond. *Nat. Commun.* **3**, 729 (2012).
12. A. Lozovoi, H. Jayakumar, D. Daw, A. Lakra, C. A. Meriles, Probing metastable space-charge potentials in a wide band gap semiconductor. *Phys. Rev. Lett.* **125**, 256602 (2020).
13. S. Karaveli et al., Modulation of nitrogen vacancy charge state and fluorescence in nanodiamonds using electrochemical potential. *Proc. Natl. Acad. Sci. U.S.A.* **113**, 3938–3943 (2016).
14. M. Krečmarová et al., A label-free diamond microfluidic DNA sensor based on active nitrogen-vacancy center charge state control. *ACS Appl. Mater. Interfaces* **13**, 18500–18510 (2021).
15. V. Petráková et al., Luminescence of nanodiamond driven by atomic functionalization: Towards novel detection principles. *Adv. Funct. Mater.* **22**, 812–819 (2012).
16. D. J. McCloskey et al., A diamond voltage imaging microscope. *Nat. Photonics* **16**, 730–736 (2022).
17. C. Li, S. X. L. Luo, D. M. Kim, G. Wang, P. Cappellaro, Ion sensors with crown ether-functionalized nanodiamonds (2023).
18. A. Lozovoi et al., Optical activation and detection of charge transport between individual colour centres in diamond. *Nat. Elect.* **4**, 717–724 (2021).
19. H. Jayakumar et al., Optical patterning of trapped charge in nitrogen-doped diamond. *Nat. Commun.* **7**, 12660 (2016).
20. A. Lozovoi, D. Daw, H. Jayakumar, C. A. Meriles, Dark defect charge dynamics in bulk chemical-vapor-deposition-grown diamonds probed via nitrogen vacancy centers. *Phys. Rev. Mater.* **4**, 053602 (2020).
21. A. Lozovoi, G. Vizkelethy, E. Bielejec, Imaging dark charge emitters in diamond via carrier-to-photon conversion. *Sci. Adv.* **8**, eabl9402 (2022).
22. H. Jayakumar, S. Dhomkar, J. Henshaw, C. A. Meriles, Spin readout via spin-to-charge conversion in bulk diamond nitrogen-vacancy ensembles. *Appl. Phys. Lett.* **113**, 122404 (2018).
23. B. J. Shields, Q. P. Unterreithmeier, N. P. de Leon, H. Park, M. D. Lukin, Efficient readout of a single spin state in diamond via spin-to-charge conversion. *Phys. Rev. Lett.* **114**, 136402 (2015).
24. Q. Zhang et al., High-fidelity single-shot readout of single electron spin in diamond with spin-to-charge conversion. *Nat. Commun.* **12**, 1529 (2021).
25. C. V. Peaker, First principles study of point defects in diamond (2018).
26. L. S. Pan, D. R. Kania, P. Pianetta, O. L. Landen, Carrier density dependent photoconductivity in diamond. *Appl. Phys. Lett.* **57**, 623–625 (1990).
27. A. M. Edmonds et al., Production of oriented nitrogen-vacancy color centers in synthetic diamond. *Phys. Rev. B* **86**, 035201 (2012).
28. G. Wang et al., Fast wide-field quantum sensor based on solid-state spins integrated with a SPAD array. *Adv. Quantum Technol.*, 230046 (2023).
29. F. Madonini, F. Severini, F. Zappa, F. Villa, Single photon Avalanche diode arrays for quantum imaging and microscopy. *Adv. Quant. Technol.* **4**, 2100005 (2021).
30. D. Bronzi et al., 100 000 frames/s 64 × 32 single-photon detector array for 2-D imaging and 3-D ranging. *IEEE J. Select. Topics Quant. Elect.* **20**, 355–364 (2014).
31. S. Li et al., Determination of local defect density in diamond by double electron-electron resonance. *Phys. Rev. B* **104**, 094307 (2021).
32. V. Stepanov, S. Takahashi, Determination of nitrogen spin concentration in diamond using double electron-electron resonance. *Phys. Rev. B* **94**, 024421 (2016).
33. E. Bauch et al., Decoherence of ensembles of nitrogen-vacancy centers in diamond. *Phys. Rev. B* **102**, 134210 (2020).
34. W. K. C. Sun, P. Cappellaro, Self-consistent noise characterization of quantum devices. *Phys. Rev. B* **106**, 155413 (2022).
35. Z. H. Wang, S. Takahashi, Spin decoherence and electron spin bath noise of a nitrogen-vacancy center in diamond. *Phys. Rev. B* **87**, 115122 (2013).
36. H. Park, J. Lee, S. Han, S. Oh, H. Seo, Decoherence of nitrogen-vacancy spin ensembles in a nitrogen electron-nuclear spin bath in diamond. *npj Quant. Inf.* **8**, 95 (2022).
37. G. Wang et al., Characterizing temperature and strain variations with qubit ensembles for their robust coherence protection. *Phys. Rev. Lett.* **131**, 043602 (2023).
38. G. Wang et al., Sensing of arbitrary-frequency fields using a quantum mixer. *Phys. Rev. X* **12**, 021061 (2022).
39. R. Cruddace, Magnetic resonance and optical studies of point defects in single crystal CVD diamond (2007).
40. M. N. R. Ashfold et al., Nitrogen in diamond. *Chem. Rev.* **120**, 5745–5794 (2020).
41. C. Glover, M. E. Newton, P. Martineau, D. J. Twitchen, J. M. Baker, Hydrogen incorporation in diamond: The nitrogen-vacancy-hydrogen complex. *Phys. Rev. Lett.* **90**, 185507 (2003).
42. J. H. N. Loubser, J. A. van Wyk, Electron spin resonance in the study of diamond. *Rep. Progr. Phys.* **41**, 1201–1248 (1978).
43. J. H. E. Griffiths, J. Owen, I. M. Ward, Paramagnetic resonance in neutron-irradiated diamond and smoky quartz. *Nature* **173**, 439–440 (1954).
44. J. A. Baldwin, Electron paramagnetic resonance investigation of the vacancy in diamond. *Phys. Rev. Lett.* **10**, 220–222 (1963).
45. C. Pellet-Mary, P. Huillery, M. Perdriat, A. Tallaire, G. Hétet, Optical detection of paramagnetic defects in diamond grown by chemical vapor deposition. *Phys. Rev. B* **103**, L100411 (2021).
46. N. Nunn et al., Electron irradiation-induced paramagnetic and fluorescent defects in type Ib high pressure-high temperature microcrystalline diamonds and their evolution upon annealing. *J. Appl. Phys.* **132**, 075106 (2022).
47. J. Isoya et al., EPR identification of the negatively charged vacancy in diamond. *Phys. Rev. B* **45**, 1436–1439 (1992).
48. E. J. Davis et al., Probing many-body noise in a strongly interacting two-dimensional dipolar spin system (2021).
49. M. W. Doherty et al., Towards a room-temperature spin quantum bus in diamond via electron photoionization, transport, and capture. *Phys. Rev. X* **6**, 041035 (2016).
50. M. J. H. Ku et al., Imaging viscous flow of the Dirac fluid in graphene. *Nature* **583**, 537–541 (2020).
51. K. Rezai, S. Choi, M. D. Lukin, A. O. Sushkov, Probing dynamics of a two-dimensional dipolar spin ensemble using single qubit sensor (2022).
52. Z. Zhang, M. Joos, D. Bluvstein, Y. Lyu, A. C. B. Jayich, Reporter-spin-assisted T1 relaxometry (2022).
53. D. M. Irber et al., Robust all-optical single-shot readout of nitrogen-vacancy centers in diamond. *Nat. Commun.* **12**, 532 (2021).
54. Z. H. Zhang, A. M. Edmonds, N. Palmer, M. L. Markham, N. P. de Leon, Neutral Silicon Vacancy Centers in Diamond via Photoactivated Itinerant Carriers (2022).
55. U. Sivan, M. Heiblum, C. P. Umbach, H. Shtrikman, Electrostatic electron lens in the ballistic regime. *Phys. Rev. B* **41**, 7937–7940 (1990).
56. R. M. Nieminen, "Supercell methods for defect calculations" in *Theory of Defects in Semiconductors* (Springer, 2007), pp. 29–68.
57. G. Kresse, J. Furthmüller, Efficient iterative schemes for ab initio total-energy calculations using a plane-wave basis set. *Phys. Rev. B* **54**, 11169 (1996).
58. G. Kresse, D. Joubert, From ultrasoft pseudopotentials to the projector augmented-wave method. *Phys. Rev. B* **59**, 1758 (1999).
59. J. P. Perdew, K. Burke, M. Ernzerhof, Generalized gradient approximation made simple. *Phys. Rev. Lett.* **77**, 3865 (1996).
60. H. J. Monkhorst, J. D. Pack, Special points for brillouin-zone integrations. *Phys. Rev. B* **13**, 5188 (1976).
61. V. Ivády, T. Simon, J. R. Maze, I. Abrikosov, A. Gali, Pressure and temperature dependence of the zero-field splitting in the ground state of NV centers in diamond: A first-principles study. *Phys. Rev. B* **90**, 235205 (2014).